The sensitivity of nocturnal low-level jets and near-surface winds over the Sahel to model resolution, initial conditions and boundary-layer set-up

K. Schepanski,[a*†] P. Knippertz,[b†] S. Fiedler,[b†] F. Timouk[c] and J. Demarty[d]

[a]*Leibniz Institute for Tropospheric Research, TROPOS, Leipzig, Germany*
[b]*Karlsruhe Institute of Technology, KIT, Karlsruhe, Germany*
[c]*Géosciences Environment Toulouse, UMR 5563, CNRS/UPS/IRD/CNES, Toulouse, France*
[d]*HydroSciences Montpellier, UMR 5569, IRD/UM2/CNRS/UM1, Montpellier, France*

*Correspondence to: K. Schepanski, Leibniz Institute for Tropospheric Research, TROPOS, 04318 Leipzig, Germany.
E-mail: schepanski@tropos.de

This study explores simulations using the numerical Weather Research and Forecasting (WRF) model, with respect to the representation of the nocturnal low-level jet (LLJ) over the Sahel. Three sets of experiments are designed to investigate the sensitivity with respect to (i) the boundary-layer and surface-layer schemes including local and non-local closures, (ii) the horizontal grid spacing and the number of vertical levels within the lowest kilometre and (iii) the role of initial and boundary data. In total, 27 simulations are performed on one host domain and two nested domains for a representative LLJ case study on 9 November 2006. The ability of the individual simulations to represent the life cycle of the nocturnal LLJ is validated against observations carried out in the framework of the African Monsoon Multidisciplinary Analysis (AMMA) special observation periods: surface wind observations from Agoufou, Bamba and Banizoumbou, atmospheric wind profiles derived from Atmospheric Radiation Measurement Mobile Facility, wind radar measurements at Niamey and profiles from radiosondes launched at Niamey. All runs reproduce the general characteristics of the observed LLJs satisfactorily. In contrast to earlier studies, results are more sensitive to the choice of initial and boundary data (here GFS and ECMWF) than to the boundary-layer and surface schemes used or to model grid resolution. The sensitivity to the model grid resolution is surprisingly minor. Considerable differences between the individual stations suggest that local surface conditions such as roughness length, albedo or soil moisture may play an important role in the observed mismatch between model simulations and observations.

Key Words: nocturnal low-level jet; regional modeling; AMMA; Sahel; WRF

1. Introduction

Low-level jets (LLJs) are phenomena observed worldwide, typically developing as a distinct wind-speed maximum within the first kilometre above the ground (Stensrud, 1996; Banta *et al.*, 2006). The classical mechanism for their formation involves an inertial oscillation around the low-level geostrophic wind in a layer that is frictionally decoupled from the surface (Blackadar, 1957). LLJs are of particular importance over North Africa, where they are found to be the dominant driver for morning-hour dust emission (Schepanski *et al.*, 2009a). In most cases, these morning dust events are initiated by increased surface wind speeds that result from the downward mixing of momentum associated with the erosion of the LLJ (Schepanski *et al.*, 2009a, 2013; Fiedler *et al.*, 2013; Heinold *et al.*, 2013; Tegen *et al.*, 2013). Once dust is emitted, LLJs are also important for the regional transport of dust (Kalu, 1979; Westphal *et al.*, 1987; Schepanski *et al.*, 2009b). In addition, LLJs are of relevance for many other aspects such as wind energy generation (Storm *et al.*, 2009), aerosol and pollutant dispersion and thus air quality (Banta *et al.*, 1998), the initiation and sustenance of deep convection (Maddox, 1983) and the migration pathways of birds and insects (Liechti and Schaller, 1999).

There are numerous observational and modelling studies linking LLJs with dust emission over the Sahara and Sahel. For example, Schepanski *et al.* (2013) describe dust emission from alluvial sources over North Mauritania during the LLJ breakdown identified from airborne lidar observations and profiles obtained

[†]Formerly at School of Earth and Environment, University of Leeds, Leeds, UK.

from dropsondes. Many authors discuss the role of the LLJ over the Bodélé Depression, Chad, for dust emission, the formation of which is favoured by the channelling effect of the Tibesti and Ennedi Massifs (e.g. Washington *et al.*, 2005, 2009; Bouet *et al.*, 2007; Todd *et al.*, 2007). Over the Sahel, favourable conditions for LLJ formation occur year-round (Schepanski *et al.*, 2009a; Fiedler *et al.*, 2013). The LLJs are embedded in the dry northeasterly Harmattan flow that results from the pressure gradient between the subtropical high and a weak heat trough over southern West Africa. During the wet season, LLJs form along the pressure gradients over the intertropical discontinuity, where monsoonal and desert air masses converge, but the increasing vegetation cover in the course of the rainy season suppresses emissions in southern areas, as shown by Knippertz (2008), Knippertz and Todd (2012) and Heinold *et al.* (2013). The aforementioned studies suggest that the accurate representation of the development and decay of the nocturnal LLJ is crucial for simulating dust emission and transport processes over arid and semi-arid regions, in particular over North Africa.

The development of a LLJ usually requires a stably stratified nocturnal boundary layer and is associated with calm conditions at the surface (Thorpe and Guymer, 1977). The conceptual model proposed by Blackadar (1957) has been extended by Van de Wiel *et al.* (2010), by accounting for frictional effects. Measurement campaigns such as the Cooperative Atmosphere–Surface Exchange Study–1999 (CASES-99) experiment (Poulos *et al.*, 2002) or the Global Energy and Water Cycle Experiment (GEWEX) Atmospheric Boundary Layer Studies (GABLS) experiments, among others, provide useful information on LLJ characteristics. Results from these field experiments also contribute to modelling studies that document and investigate possible mechanisms for LLJ development (e.g. Baas *et al.*, 2010; Gibbs *et al.*, 2011; Chiao and Dumais, 2013; Sun *et al.*, 2013; Ngan *et al.*, 2013). Besides the inertial oscillation mechanism, LLJ formation may be forced by synoptic-scale baroclinity that can be associated with e.g. fronts, sloping terrain, ducting and confluence around mountain barriers, land–sea breezes or mountain-valley circulations. In the remainder of this study, we will focus on the LLJ formation related to inertial oscillation. The life cycle of a nocturnal LLJ is determined by four key elements, each influenced by surface and boundary-layer characteristics such as atmospheric stability, surface roughness, soil moisture, soil characteristics and albedo.

(1) *Initial conditions*. The conditions during the afternoon determine the starting point for the inertial oscillation, the amplitude of which depends strongly on the magnitude of the ageostrophic component of the wind. The phase of the oscillation depends on the angle between the geostrophic and actual winds. These are determined by the background pressure gradient, the Coriolis parameter f (and thus latitude) and surface friction.
(2) *Decoupling*. After sunset, radiative cooling forms a stably stratified nocturnal boundary layer, often capped by a temperature inversion that separates the surface layer from the residual layer. The cooling depends strongly on parameters such as cloud cover, column water vapour or aerosols, while the timing depends on the length of day and therefore the season. The inversion decouples the air within the residual layer from surface friction, which results in acceleration. The duration and degree of decoupling depend strongly on the boundary-layer stability. If decoupling persists through the night, an almost perfect inertial oscillation can be observed. If shear underneath the LLJ exceeds a critical value, intermittent turbulence can occur, which weakens the jet and enhances surface winds.
(3) *Inertial oscillation*. The inertial oscillation represents the rotation of the ageostrophic wind component around the geostrophic (balanced) wind. Its period is given by $2\pi/f$. In areas where the length of the decoupling period is similar to half an inertial period, supergeostrophic wind velocities can occur during the morning, making the Sahel and southern Sahara a prominent location for LLJ formation.
(4) *Decay*. The breakdown of a LLJ usually begins after sunrise, when solar radiation fosters the deepening of the convective boundary layer. Once mixing has eroded the surface temperature inversion, high momentum from the LLJ can be transported to the surface, triggering dust emission over areas with deflatable material. The timing and characteristics of the decay depend strongly on the boundary-layer stability in the morning and the amount of solar heating.

From a modelling perspective, the four key points listed above all need to be well represented to reproduce the life cycle of the nocturnal LLJ accurately. The initiation phase requires a realistic representation of the background pressure gradient and friction to represent the ageostrophic wind component in the afternoon correctly. The decoupling will be sensitive to the model turbulence and flux schemes and thus to the applied boundary-layer scheme and surface conditions. The actual inertial oscillation is handled by the dynamical core of the model and we do not expect this to be a major source of error, as previous case studies have shown successful simulations of inertial oscillation in other regions (e.g. Storm and Basu, 2010; Giannakopoulou and Toumi, 2012). The correct simulation of near-surface winds during the breakdown of the LLJ requires an accurate representation of LLJ strength and core height and atmospheric stability in the morning and therefore depends on the first three key elements. In addition, the erosion of the LLJ through turbulent downward mixing needs to be simulated realistically, depending on both the boundary-layer scheme and the surface roughness. Also, soil moisture and albedo can influence the LLJ and surface wind evolution through their effects on the surface energy balance, which affects the Bowen ratio and can impact on both the state of the boundary layer before the evening transition and the morning breakdown.

Results from studies using mesoscale models to simulate synoptic situations favouring the nocturnal LLJ development generally reproduce the large-scale pressure gradients that drive LLJs satisfactorily and capture the LLJ life cycle. However, model studies using different boundary-layer/surface-layer set-ups show diverse results concerning the accurate representation of LLJ core wind speed and LLJ core height, which may lead to errors in the diurnal cycle of near-surface winds (e.g. Storm *et al.*, 2009; Hu *et al.*, 2010, 2013). The main reason discussed is too much mixing within the boundary layer during stable night-time conditions, leading to too weak temperature inversions and too little decoupling (Hanna and Yang, 2001; Zhong and Fast, 2003). This suggests a sensitivity of the representation of the nocturnal LLJ to boundary-layer parametrization, which is ultimately affected by vertical grid resolution and the accuracy of surface characteristics such as roughness length, soil moisture and vegetation.

In order to help our understanding of the ability of numerical models to capture the nocturnal LLJ phenomenon, this study aims to test the sensitivity of a commonly used mesoscale model in its ability to simulate the life cycle of a nocturnal LLJ with regard to the following.

(1) *Initial and boundary data*, as the generation of a background pressure gradient is crucial for the initial conditions of LLJ formation (cf. description of LLJ life cycle above).
(2) *Boundary-layer (BL) and surface-layer (SL) scheme*, as the accurate parametrization of BL dynamics is crucial for simulating the decoupling of the residual layer from the nocturnal BL, in order to allow for the acceleration of the LLJ layer (inertial oscillation) and ultimately its breakdown during the following morning.
(3) *Horizontal and vertical grid resolution*, as this is hypothesized to be crucial for capturing inversion layers and horizontal inhomogeneity, resulting in pressure gradients

that may support or suppress frictional decoupling of the nocturnal BL from the layers aloft.

To examine the above-mentioned factors affecting the accuracy of a model's ability to represent the life cycle of a nocturnal LLJ, a case study is performed using the mesoscale Weather Research and Forecasting (WRF) model (Skamarock *et al.*, 2008; cf. section 2.2). As the representation of the nocturnal LLJ is well studied for midlatitudinal conditions such as for Cabauw, the Netherlands (e.g. Kleczek *et al.*, 2014), this study focuses on the development and decay of nocturnal LLJs over the Sahel during the dry season. During this time of year, the Sahel zone exemplarily stands for a region with a predominant pressure gradient between the tropical trough to the south and the subtropical high-pressure zone to the north, resulting in northeasterly near-surface winds, the Harmattan. Due to low latitudes, the period of the inertial oscillation forming the LLJ is longer than at midlatitudes. Furthermore, over the Sahel region, operational surface observations are sparse and thus boundary and initial conditions taken from global atmosphere models for driving the WRF model at the mesoscale may differ. Throughout the discussion, we will refer to the conceptual model of the LLJ life cycle, consisting of the four elements 'initial conditions', 'decoupling', 'inertial oscillation' and 'decay' as introduced above.

The remainder of this article is structured in the following way: section 2 provides an overview of the data used and a description of the model and numerical experiments. Evidence for LLJ formation in both observations and model fields is presented in section 3. Results from WRF sensitivity experiments are given and evaluated against observations in section 4. The results are discussed in section 5, followed by concluding remarks.

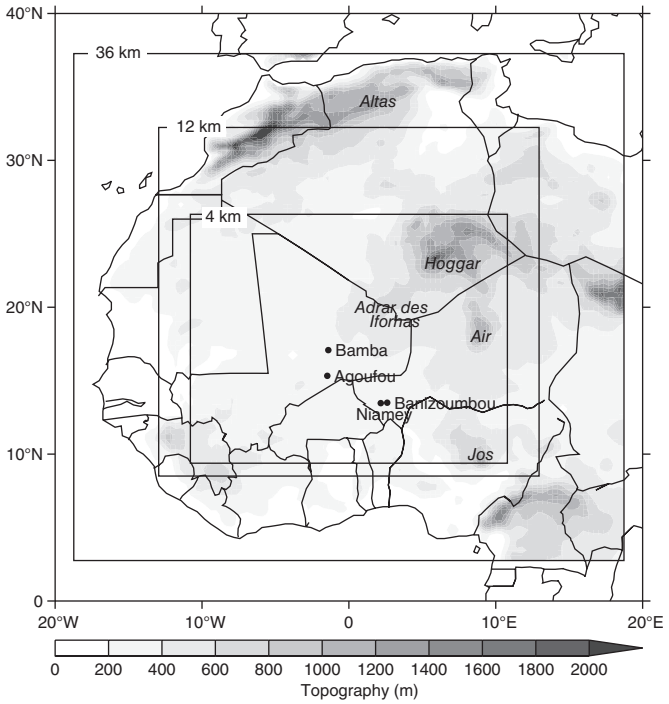

Figure 1. Geographic overview of the outer model domain (36 km grid spacing) and nesting (12 and 4 km grid spacing) used for the different experiments, as outlined in section 2 and Table 1. Filled circles indicate the geographic location of the observation sites. Geographic names for mountain regions lying within the model domain are given in italics.

2. Data and model description

The Sahel and Sahara are chosen as a region of particular interest for this study, since nocturnal LLJs occur frequently during the dry season (November–February) and are often associated with dust emission (Schepanski *et al.*, 2009a; Fiedler *et al.*, 2013; Tegen *et al.*, 2013). The study region covers the area 10°W–10°E and 10–25°N, as shown in Figure 1. Observations from the meteorological sites at Agoufou, Bamba, Banizoumbou and Niamey (locations shown in Figure 1) are used here in order to characterize the LLJ development and to assess the model simulations. Details on the observations used within this study and a description of the WRF model set-ups are provided within the following sections 2.1 and 2.2.

2.1. *Observations*

The stations Agoufou (15.33°N, 1.47°W; 290 m above sea level) and Bamba (17.08°N, 1.4°W; 280 m above sea level) in Mali are part of the Gourma observation site (Mougin *et al.*, 2009) embedded in the African Monsoon Multidisciplinary Analysis (AMMA: Redelsperger *et al.*, 2006) observation network. The Gourma site is characterized by a semi-arid climate with high maximum temperatures and strong annual and interannual precipitation variability, with most rains occurring during the monsoon season from June–September. The northeasterly Harmattan is the dominant wind regime during the dry season. Both stations were equipped with an A100R Vector anemometer and a W200P Vector wind vane to measure wind speed and direction with a nominal data acquisition time step of 1 min and an accuracy of 0.1 m s^{-1} for the anemometer and an accuracy of 2° for the wind vane. The data analyzed here were averaged over 15 min and provided at this temporal resolution through the AMMA data base.[§]

The observation site nearby Banizoumbou (13.5°N, 2.61°E; 211 m above sea level), Niger, is one of the AMMA–Catch observation sites in Niger (Cappelaere *et al.*, 2009). Wind measurements are performed using a Windsonic 2-D instrument and are available through the AMMA data base at 15 min resolution.

The Atmospheric Radiation Measurement (ARM) mobile facility was deployed at the Niger Meteorological Office at Niamey International Airport (13.47°N, 2.17°E; 205 m above sea level) during 2006 as part of the AMMA special observing periods (SOPs) and the Radiative Divergence using the ARM Mobile Facility (AMF), the Global Earth Radiation Budget (GERB) and AMMA Stations (RADAGAST) field campaign (Slingo *et al.*, 2008). A description of the instruments can be found in Miller and Slingo (2007). In this study, surface meteorology and profiles of horizontal wind fields obtained from the three-beam Doppler UHF operated at 1040 MHz (wind radar) were used to characterize the vertical wind speed distribution. Data were available at 1 h time intervals with a vertical resolution of 75 m, with the lowest level at 87 m above ground level (Miller and Slingo, 2007). Near-surface wind speeds were measured at 1 min acquisition time-steps by a Vaisala WAA251 cup anemometer installed at 2 m above ground level. In addition, vertical profiles from radiosondes (Vaisala model RS-92) launched at Niamey (13.47°N 2.17°E; 205 m above sea level) were analyzed. During the sounding, data were acquired at intervals of 2 s.

Since the height of the anemometers at the stations is 3 m (Agoufou and Bamba) and 2 m (Banizoumbou and Niamey), WRF 10 m wind speeds were converted to wind speeds u that can be expected at anemometer height. The relation of the vertical wind speed distribution depending on the atmospheric stability can be expressed by (Stull, 1989)

$$u = \frac{u_*}{\kappa}\left[\ln\left(\frac{z}{z_0}\right) - \Psi_\mathrm{m}\left(\frac{z}{L}\right) + \Psi_\mathrm{m}\left(\frac{z_0}{L}\right)\right], \qquad (1)$$

with u_* the wind friction velocity, κ the von Kármán constant, here $\kappa = 0.41$, z the height of the anemometer above ground level, z_0 the aerodynamic roughness length, Ψ the wind shear and L the Obukhov length. Here, z_0 is taken from the MM5-28 model simulation and assumed to be temporally constant:

[§]http://database.amma-international.org

0.107 553 m for Agoufou, 0.01 m for Bamba and 0.112 937 m for Banizoumbou.

2.2. WRF simulations

2.2.1. Model description

The WRF model (Skamarock *et al.*, 2008) is a mesoscale model that is widely used to investigate and forecast a wide range of atmospheric phenomena, to examine the response of the atmosphere to different environmental conditions and to assess the representation of atmospheric features in comparison with observations (e.g. Zhang and Zheng, 2004; Li and Pu, 2008; Storm and Basu, 2010; Horvath *et al.*, 2012; Hu *et al.*, 2012; Xie *et al.*, 2013; Yang *et al.*, 2013; Yver *et al.*, 2013). Many different parametrization schemes are implemented in WRF to allow sensitivity studies and to foster model development (e.g. Gilliam *et al.*, 2009; Hu *et al.*, 2010; Nielsen-Gammon *et al.*, 2010; Gibbs *et al.*, 2011; Horvath *et al.*, 2012). In its set-up for regional scales, WRF requires atmospheric initial and boundary data, typically obtained from global atmospheric circulation models or reanalysis products. Although the spin-up allows the model to develop its own stable fields in the interior of the domain, initial conditions may impact the simulation well beyond the spin-up time, as shown by Kothe *et al.* (2013) using the COSMO-CLM model to investigate the West African monsoon system. Similar sensitivities are found by Menut (2008), quantifying the impact of the chosen reanalysis datasets for simulating the mineral dust emission flux over North Africa.

WRF simulations performed for this study use WRF version 3.3. As the representation of the life cycle of the nocturnal LLJ is in the focus of this study, two different types of BL similarities are tested: 'non-local' and 'local' similarities (cf. section 2.2.2). Schemes for microphysics, cloud parametrization, radiation and land surface are chosen with regard to appropriateness following the comprehensive sensitivity study by Borge *et al.* (2008) and are not changed throughout the experiments within this study. The WRF set-up includes the single-moment three-class microphysics scheme, the Grell–Devenyi ensemble Scheme for cumulus parametrization (simulations using grid spacings of 36 and 12 km only), the Dudhia scheme (Dudhia, 1989) for short-wave radiation, the Rapid Radiative Transfer Model (RRTM: Mlawer *et al.*, 1997) for long-wave radiation and the Noah land surface model (LSM: Chen and Dudhia, 2001). A spin-up time of 12 h is given and the model top level is at 50 hPa. The simulations are run on three one-way nested domains with 36 km (110×110 grid cells, outer domain), 12 km (226×223 grid cells, first nest) and 4 km horizontal grid spacings (562×446 grid cells, innermost nest), as shown in Figure 1. An overview of the model set-ups and experiments is given in Table 1.

2.2.2. Sensitivity experiments

The aim of the presented sensitivity study is to test the representation of the nocturnal LLJ over the Sahel for different WRF set-ups. Therefore, three sets of experiments are carried out: (1) different BL schemes (local and non-local) and SL similarities; (2) different initial and boundary data; and (3) different numbers of vertical levels within the first kilometre above ground level. The sensitivity to horizontal resolution is assessed using the three nested grids described above. The detailed set-ups of these groups of experiments are as follows.

(1) Two different BL schemes and three different SL similarities are combined. For this study, two BL are chosen as examples representing the two main types of BL parametrization: 'non-local' (first-order closure) and 'local' (turbulent kinetic energy (TKE) closure) schemes. The main characteristics of a first-order closure similarity are that these schemes do not require any additional prognostic equations to parametrize the effects of turbulence on mean variables and that the calculation of the diffusivity term within the BL is a function of local wind shear and the Richardson number in the free atmosphere. TKE closure (also named one-and-a-half order) similarities require additional prognostic equations for TKE. Thereby, local mixing is determined by local diffusivity estimated from the lowest to the highest vertical BL level. No separation between the planetary boundary layer (PBL) and the free atmosphere is considered. A more detailed review of the diffferent types of PBL similarity can be found in Shin and Hong (2011) and references therein.
In this study, the widely used non-local Asymmetric Convective Model (ACM2: Pleim, 2007) and the local Mellor–Yamada–Janjic model (MYJ: Janjic *et al.*, 2001) are applied representatively for the two different PBL similarity classes. The BL schemes are coupled to SL schemes for the calculation of surface exchange coefficients to determine heat and momentum fluxes. The following pairings of BL schemes and SL similarities are made: ACM2–MM5 (Paulson, 1970; Pleim, 2007), ACM2–PX (Pleim, 2006, 2007) and MYJ–ETA (Janjic *et al.*, 2001, cf. Table 1). Only ACM2 can be run with two different SL similarities for WRF version 3.3.

(2) The contribution of the choice of the initial and boundary data to the model's sensitivity in representing the nocturnal LLJ is evaluated. This is realized by initializing the three different WRF BL/SL set-ups with two commonly used global datasets: the European Centre for Medium-Range Weather Forecasts (ECMWF) ERA-Interim reanalysis (Dee *et al.*, 2011) and the National Oceanic and Atmospheric Administration (NOAA) Global Forecast System (GFS) analysis fields. Both datasets were used on $1^\circ \times 1^\circ$ horizontal grid spacing and six-hourly temporal resolution to drive the individual WRF set-ups (cf. Table 1).

(3) Three different sets of vertical grids are tested. As we expect LLJ cores to occur at heights of about 300–700 m above ground level (Fiedler *et al.*, 2013), the number of vertical levels is increased within the lowest kilometre of the atmosphere only. Throughout the experiments, terrain-following sigma levels are used. Starting with the standard configuration of eight levels (28 levels in total; lowest sigma level at around 64 m above ground level (agl)) depending on ground level height, the number was increased to 15 levels (41 levels in total; lowest level at around 26 m agl) and 29 levels (60 levels in total; lowest level at around 13 m agl).

2.3. Objective identification of LLJs

In order to identify LLJs objectively in the different model runs, the algorithm developed by Fiedler *et al.* (2013) for ECMWF ERA-Interim reanalysis data was adapted to match the requirements of mesoscale data fields. In particular, due to the finer grid spacing in WRF, it can be assumed that the life cycle of the nocturnal LLJ is resolved in more detail. Since nocturnal LLJs are observed to form close to the surface, the LLJ identification is limited to the lowest 1500 m above ground level. Only wind speed maxima above the surface layer will be considered. Since LLJs form during calm wind conditions and above or respectively close to the top of a stably stratified boundary layer, the lapse rate calculated using the virtual potential temperature is required to be above 1.5 K per 100 m. The wind speed above the LLJ core must decrease to form the characteristic low-level maximum, often referred to as the 'nose' in vertical profiles of wind speeds. Here, the vertical shear within 1000 m above the LLJ core has to exceed $0.5\,\mathrm{m\,s^{-1}}$ per 100 m. Adapted thresholds were kept fixed for all WRF experiments. An extensive sensitivity test on the algorithm can be found in Fiedler *et al.* (2013).

Table 1. Overview of WRF model set-ups.

Set-up	BL scheme	SL scheme	Vertical levels	Lowest levels (m agl)
MM5-28	Asymmetric Convective Model (ACM2)	MM5	28	64
PX-28	Asymmetric Convective Model, (ACM2)	Pleim-Xiu (PX)	28	64
ETA-28	Mellor–Yamada–Janjic (MYJ)	ETA	28	64
MM5-41	Asymmetric Convective Model (ACM2)	MM5	41	26
PX-41	Asymmetric Convective Model (ACM2)	Pleim-Xiu (PX)	41	26
ETA-41	Mellor–Yamada–Janjic (MYJ)	ETA	41	26
MM5-60	Asymmetric Convective Model (ACM2)	MM5	60	13
PX-60	Asymmetric Convective Model (ACM2)	Pleim-Xiu (PX)	60	13
ETA-60	Mellor–Yamada–Janjic (MYJ)	ETA	60	13

3. Evidence for LLJ formation in model fields and observations

In order to test the influence of different model set-ups on the representation of the life cycle of the nocturnal LLJ over the Sahel, a typical event occurring on 9 November 2006 is chosen as a representative case study. In the following subsections, evidence for LLJ formation in both model fields and observations is presented and geographical variations are discussed.

The atmospheric circulation over North Africa during this dry season case study is determined by a pressure gradient between high values over the central Mediterranean Sea and low values over southern West Africa shown as geopotential heights at 925 hPa in Figure 2(a). Such a pressure gradient and resulting northeasterly Harmattan flow over North Africa are characteristic of the dry season over the Sahel, when nocturnal LLJs frequently occur (Schepanski *et al.*, 2009a).

The anomaly with respect to the 2005–2008 November mean (Figure 2(b)) reveals that the case under study is characterized to first order by an enhancement of the climatological gradient with higher than normal geopotential height in the northeast of the domain and small anomalies elsewhere. Comparing those anomalies with standard deviations for the same period (Figure 2(c)) shows that the deviation from the mean is of the order of 1–2 sigma, making it an unusual but not extreme case. The case selected therefore appears to be a good representative for situations of moderately enhanced Harmattan winds over large parts of the Sahara and Sahel.

3.1. Observations

The observation sites at Agoufou, Bamba, Banizoumbou and Niamey are all situated within the area of moderate south-west–northeast gradients of geopotential height (Figure 2(a)), associated with the Harmattan flow. The radiosonde profile from Niamey at 0000 UTC (Figure 3(a)) shows clear indications of LLJ formation. Over Niamey, a low-level wind speed maximum of 10.5 m s^{-1} is observed just below 200 m above ground, straddled by considerably weaker wind speeds above and below. There is a substantial underestimation of winds throughout the lowest 2000 m of the atmosphere in both ERA-Interim and GFS, with no clear indications for LLJs. This can be expected to impact on the higher-resolution WRF simulations, as discussed in section 4.

Measurements from the ARM wind radar with 1 h resolution (Figure 3(b)) allow us to document the full life cycle of the LLJ (see section 1) for Niamey. The observations for midnight are largely consistent with the radiosonde (Figure 3(a)), showing values just above 10 m s^{-1} around 200 m. In the course of the night, the LLJ accelerates rapidly to values of more than 19 m s^{-1} around sunrise, accompanied by the typical lifting of the LLJ core to about 500 m. The local minimum at 0600 UTC is suspected to be an artefact of the post-processing, but no confirmation for this could be found in the data description.

Effects on surface winds resulting from the LLJ life cycle introduced in section 1 are shown in Figure 3(c). In the early parts of the night, the surface layer appears to be decoupled and wind speeds are low. The formation of the LLJ indicated by wind speed acceleration within the LLJ layer starts around midnight. The first mixing event at 0200 UTC leads to an increase of surface wind speed, followed by a more sustained increase after 0500 UTC. After sunrise, the erosion of the jet and thus the transition to turbulent daytime conditions starts between 0700 and 0800 UTC. Surface wind speeds increase rapidly and then stay fairly constant (6 m s^{-1}) during the day, with peaks just above 9 m s^{-1}. The variability in 10 m wind speed is generally higher during the day than during the night, which is due to the presence of larger turbulence elements within the convective daytime boundary layer compared with the stable nocturnal boundary layer. The increased wind speed and its temporal fluctuations during the day are related to the turbulent downward mixing of the LLJ and thermals that develop within the convective daytime boundary layer. A fairly smooth evening transition back to calmer conditions occurs around 1800 UTC.

Figure 4 shows the diurnal cycle of wind speed for the three stations Agoufou, Bamba and Banizoumbou, together with November mean and standard deviation values for 2005–2008. The measurements of 9 November 2006 are mostly above the long-term mean wind, but within the 2 sigma envelope around the mean and consistent with the discussion of Figure 2 above. The most striking difference at all three stations is a tendency to earlier morning LLJ breakdown and higher wind speeds during the day. This demonstrates that, while this case is still representative of November conditions in general, it is likely a situation associated with dust emission from the above-average winds.

Agoufou shows a fairly similar diurnal evolution with regular fluctuations ($\pm$0.3 m s^{-1}) around about 1 m s^{-1} during the night, a sharp increase in the morning, a flat distribution during the day and a drop-off around sunset (Figure 4(a)). The maximum at Agoufou is about 6 m s^{-1} around 1000 UTC. The northernmost station Bamba shows a markedly different behaviour (Figure 4(b)), despite a rather similar background pressure gradient and therefore geostrophic wind (Figure 2(a)). With values between 2 and 4 m s^{-1}, wind speeds remain fairly high throughout the night, again showing regular fluctuations in mixing. Earlier than at the other stations, around 0600 UTC, a sharp increase is observed, leading to values of about 10 m s^{-1}, but then a gradual decline occurs throughout the day followed by a much smoother evening transition. Banizoumbou shows much weaker winds during the night, suggesting a stronger decoupling (Figure 4(c)). Initial LLJ breakdown occurs between 0700 and 0800 UTC, with an intermittent and strong burst at 0500 UTC. Maximum values reach only 4 m s^{-1} and stay fairly constant during the day. The evening transition starts at around 1800 UTC. The discrepancies between Niamey and Banizoumbou are likely due to local differences in roughness and possibly stability, which modify the LLJ and surface-wind behaviour. A detailed comparison between the model and observations will be given in section 4.

Overall, the observations discussed here suggest an important role for rather small-scale differences in surface characteristics such as roughness and albedo, possibly resulting in differences in stability, to modify LLJ and surface-wind behaviour. To address this in detail, further investigations beyond this study are required.

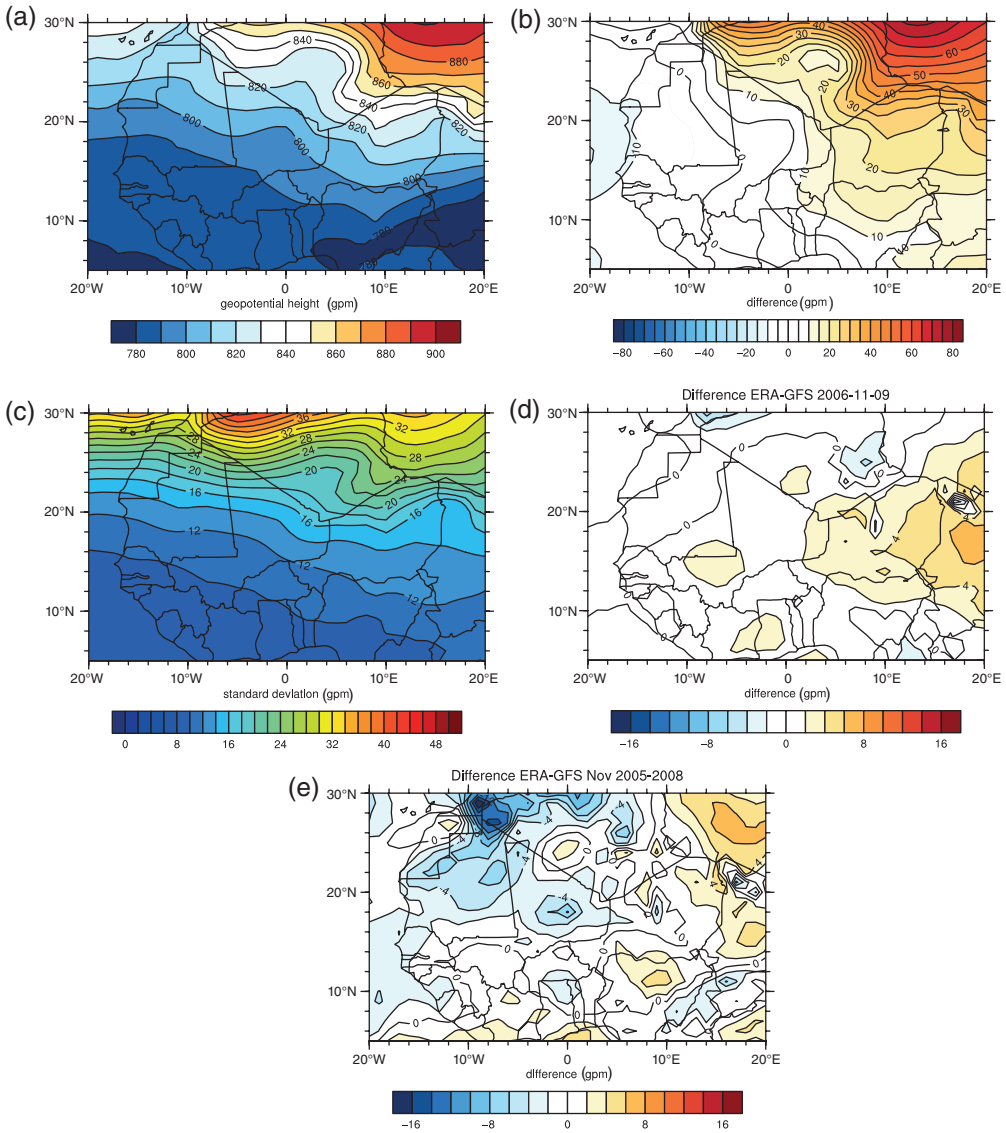

Figure 2. (a) Geopotential height (gpm) at 925 hPa for 9 November 2006, 0000 UTC from ERA-Interim data. (b) Anomaly of geopotential height (gpm) at 925 hPa for 9 November 2006, 0000 UTC compared with 2005–2008 November mean for ERA-Interim. (c) Standard deviation of ERA November 2005–2008 as parameter for temporal variability range. (d) ERA minus GFS for 9 November 2006. (e) ERA minus GFS for November 2005–2008.

3.2. *Model simulations*

The objective LLJ identification algorithm by Fiedler *et al.* (2013) as introduced in section 2.3 is applied to all WRF simulations performed for this study. As the results are not too dissimilar, the PX-41 set-up driven with ERA-Interim and run at 12 km horizontal grid spacing is chosen and discussed as an example in the following.

As shown in Figure 5, LLJs are found over large parts of the study region, but core wind speeds vary considerably from about 10 m s^{-1} in the south of the domain to well over 20 m s^{-1} to the southeast of Niamey. No LLJs are identified over the southwestern part of the domain, where pressure gradients are weak (Figure 2(a)), as well as over the higher elevated ground of the Hoggar Mountains (white areas in Figure 5(a)). Relatively high LLJ core speeds are also found to the immediate west of the Adrar des Iforhas and Hoggar Mountains (see isohypses given as black lines in Figure 5(a)). Some of the fine structure in LLJ occurrence and strength appears to be related to the deflection of low-level flow around the western part of the Hoggar Massif, with a local minimum in LLJ core speeds in the weak mostly north–south oriented convergence zone to the north of Bamba. Particularly in the west of the domain, the sharp boundary between well-developed LLJs and low winds is reminiscent of the Harmattan front discussed by Burton *et al.* (2013). Variations of LLJ core height are less pronounced, with most values around 200 m above ground (Figure 5(b)). Also, some LLJs in the region south of 12°N and east of 2°W appear to be somewhat elevated compared with the LLJ identified over the rest of the domain discussed. This may be due to the adjacency of the intertropical discontinuity zone marking the border between dry desert air masses and moist monsoonal air masses. More stable nocturnal conditions are expected for the former.

The downward turbulent transport and consequent increase in surface wind speed starts suddenly, as suggested by wind speed measurements, and lasts for several hours (Figure 4) until the late morning. Thus, the 0900 UTC time slot is found to be a good indicator for surface wind speed increase due to the LLJ breakdown. A general increase of wind speed between 0600 and 0900 UTC over the entire domain is evident (Figure 5(c) and (d)) and indicates the development of a convective boundary layer and possibly a breakdown of nocturnal LLJs. Several areas with different behaviour can be distinguished. (i) Over the higher ground in the very northeast of the domain, winds are generally strongest, but there are no clear signs of LLJs (Figure 5(a)). Most likely, the many orographic features of the Hoggar Massif in this region do not allow the undisturbed evolution of a stable nocturnal boundary layer. (ii) In the southwest corner, on the tropical side of the 'Harmattan front', pressure gradients and winds at the surface and jet level are rather weak. (iii) As expected from the introduction of the LLJ life cycle (cf. section 1), the areas with strong LLJ cores ($\geq$16 m s^{-1}; Figure 5(a)) do generally show

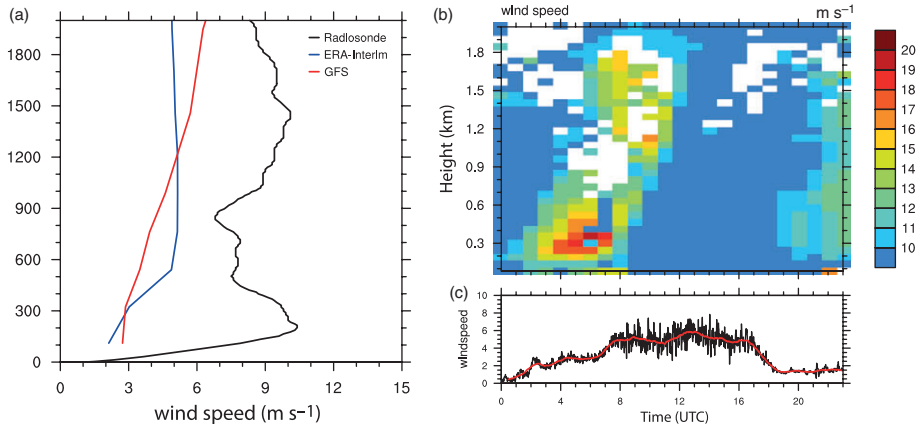

Figure 3. (a) Wind profiles obtained from the radiosonde (black) launched at Niamey on 9 November 2006, 0000 UTC and wind profiles extracted from ERA-Interim (blue in the online article) and GFS (red in the online article) for the corresponding grid box and time. (b) Vertical distribution of wind speed obtained from measurements by the ARM 1040 MHz wind radar profiler based at Niamey Airport for 9 November 2006. Lowest level 87 m above ground; vertical grid spacing 75 m; data are shown at 1 h resolution. (c) Three metre wind speeds at the same site for the same period at 1 min resolution (black) and one-hourly running mean (red in the online article).

the largest increase in wind speed between 0600 and 0900 UTC, consistent with a jet breakdown. Interestingly, this behaviour is more pronounced in the north than the south, suggesting a quicker build-up of the convective boundary layer. It appears plausible that this could be related to more evapotranspiration in southern areas relatively shortly after the end of the rainy season in the Sahel. Additionally, the dry Harmattan flow, which favours the formation of nocturnal LLJs, is stronger over the northern part. All these characteristics are consistent with an area of weaker stability, increased surface roughness due to vegetation and thus weaker decoupling in the south. Consequently, there are considerable variations in the relationship between LLJ core speed and height at 0600 UTC and associated 10 m wind at 0900 UTC between the different parts of the domain. This is the reason why there is not a simple relationship between LLJ speed and height.

4. Sensitivity experiments and model evaluation

In this section, the different sensitivity experiments will be compared with each other and with the available observations, building on the more general discussion in section 3. The first section concentrates on the broad influence of initial and boundary data. Sections 4.2 and 4.3 look more closely at differences between different resolutions and set-ups and how those compare with observations using Taylor diagrams and other evaluation techniques.

4.1. Influence of initial and boundary data

The influence of the initial and boundary data on the representation of the nocturnal LLJ is examined with two commonly used global datasets: the NOAA GFS analysis and ECMWF ERA-Interim reanalysis (see section 2.2.2). The two initial and boundary data sets are taken from two different models, which are consequently using different parametrization schemes and dynamical cores, are running at different grids with different time steps and are using different assimilation schemes. The difference between ERA-Interim and GFS input fields is illustrated in Figure 2(d). The most striking feature is a large area stretching from eastern Mali to the eastern edge of the domain, where the geopotential height at 925 hPa in ERA-Interim is between 2 and 6 gpm higher than in GFS. This corresponds to almost half a standard deviation of long-term November variations (Figure 2(c)), demonstrating a substantial disagreement between the two datasets. Given the overall situation shown in Figure 2(a), this difference implies a southward extension of the area of high geopotential over the Mediterranean Sea farther into Africa. The impact of these differences on the LLJs and near-surface winds will be discussed in sections 4.2 and 4.3. Figure 2(e) shows the long-term mean differences in 925 hPa geopotential height (November 2005–2008), illustrating the abnormality of such a large difference between the two analysis products. Generally, a negative difference is evident over the northwestern and western parts of the Sahara, whereas a positive difference is shown for the northeastern region. Comparing the difference for the case study (Figure 2(d)) with the multi-annual difference shown in Figure 2(e), the above-mentioned ridge of higher ERA-Interim geopotential heights compared with GFS values is less pronounced. The distribution of the difference in geopotential heights is dominated by a dipole between the northwestern part of the Sahara (strong negative values of about −16 gpm), with ERA-Interim geopotential heights being smaller than the GFS heights, and Libya, with larger values (up to 6 gpm) for the ERA-Interim fields than the GFS fields. Nevertheless, both distribution patterns generally agree on a tendency of lower values for ERA-Interim over the western part and higher values for ERA-Interim over the eastern part.

The mean sea-level pressure (mslp) distributions simulated by the individual runs are quite similar, but parts of the bias between ERA and GFS input fields are still present in the WRF simulations (not shown). Figure 6 shows the difference in set-up mean mslp between the simulations initiated with ERA-Interim and those initiated with GFS data, run at 36 km horizontal grid spacing with 28 levels. Results for the 41 level and 60 level simulations are not shown. Generally, throughout all time steps and set-ups, the WRF simulations initialized with ERA-Interim fields show a higher mslp over the southeastern part of the domain, including Niger and Chad, but a lower mslp over the northwestern part of North Africa, mainly Morocco, North Mauritania and parts of Algeria. This is partly triggered by the input fields (cf. Figure 2), but it can also be assumed that further differences will develop throughout the simulation. Differences of both signs reach absolute values of up to 2 hPa. These rather large discrepancies are most likely the result of the sparse observational network over large parts of northern Africa, which does not provide sufficient constraints on the analysis fields.

4.2. LLJs in WRF

The distribution of objectively identified LLJ core heights and wind speeds shown in Figure 5 has already been discussed in section 3. Figure 7 presents a statistical analysis of the LLJ core wind speed and height over the area 10°W –10°E and 10–25°N in the form of box-and-whisker plots for the nine experiments listed in Table 1. All experiments show similar median core wind speeds around 15 m s^{-1} and also a similar interquartile range (Figure 7(a) and (c)). The interquartile range is generally a little larger for simulations initialized with GFS data (Figure 7(c)) than those

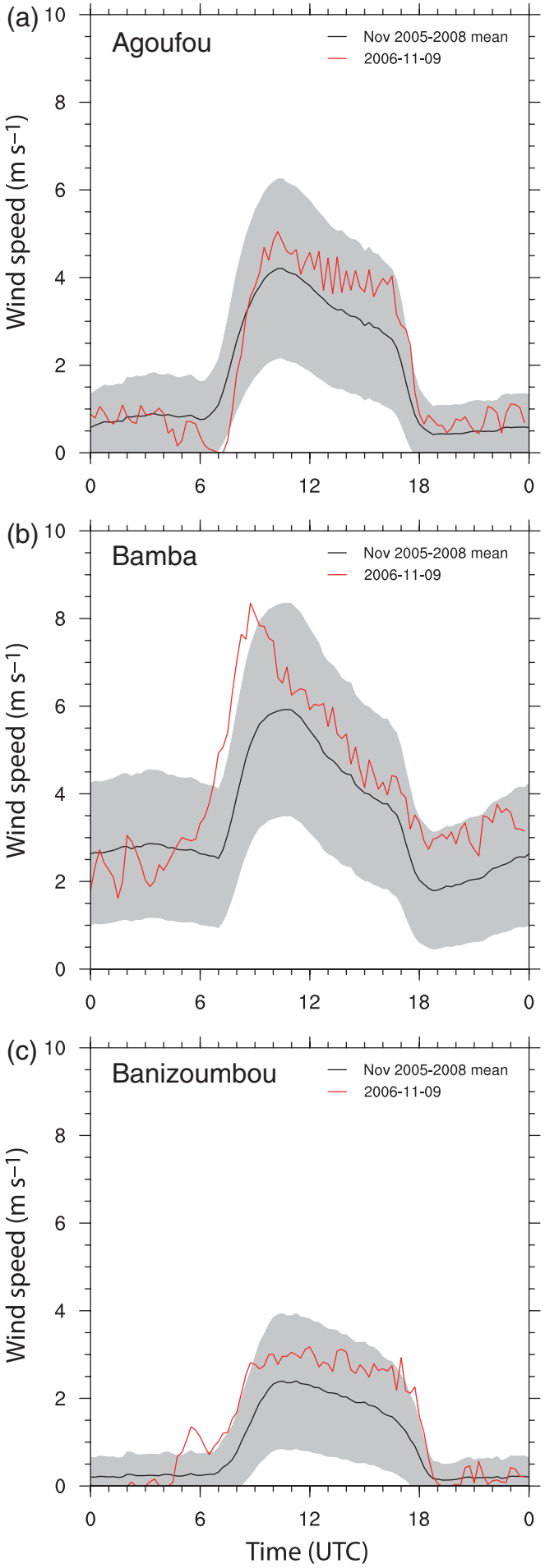

Figure 4. Diurnal cycle of near-surface wind speed for (a) Agoufou at 3 m above ground level, (b) Bamba at 3 m above ground level and (c) Banizoumbou at 2 m above ground level. The shaded area indicates the σ range for the period 2005–2008 (November only).

using ERA-Interim fields (Figure 7(a)), but overall the differences documented in Figure 6 do not have a large impact on domain statistics, most likely due to cancellation effects. Variations with regard to height are somewhat more pronounced, with medians ranging between about 200 and 250 m (Figure 7(b) and (d)). However, the box-and-whisker plots are quite skewed in some cases, partly due to the predefined number of levels in the model. There is a weak tendency for higher jet cores in runs using GFS data (Figure 7(d)).

To illustrate this further, Figure 8 shows as an example the vertical wind and potential temperature distribution and the corresponding 10 m wind speed for the PX-41 12 km model simulations initialized with ERA-Interim (Figure 8(a)) and GFS (Figure 8(b)) fields, respectively, for the grid point closest to Niamey. Although the breakdown of the nocturnal LLJ is evident from the distribution of the 10 m wind speeds according to the concept of the LLJ life cycle introduced in section 1, differences in the sharpness of the sudden increase are obvious for the different set-ups (not shown). The set-up driven by ERA-Interim fields shows a smooth increase in 10 m wind speeds gradually distributed over a couple of hours. In contrast, the set-up driven by GFS data generally shows a sharper increase in 10 m wind speeds, although the morning wind peaks are weaker. Comparing the LLJ in runs initiated with ERA-Interim fields with that initiated with GFS fields, the latter shows a weaker LLJ core speed and a shallower vertical extension across all set-ups. For a given driving dataset, the vertical extension of the LLJ cores varies less than between the two driving data sets with a given BL/SL (not shown). These discrepancies are consistent with the large mslp differences in the region of Niamey evident from Figure 6 and underline the importance of the initial conditions and background geostrophic wind. Increasing the number of vertical levels has little impact on the altitude of the LLJ core, but causes a slight increase in LLJ maximum wind speed in most cases. This is likely related to a better resolved surface inversion and therefore better decoupling.

Nevertheless, the runs initialized with ERA-Interim tend to overestimate the LLJ in magnitude and core altitude in the morning hours, while GFS shows better agreement or even underestimation in some cases (Figure 8(c)). This suggests that ERA-Interim has too large a pressure gradient compared with the observations, giving overall higher wind speeds. It is interesting to note that none of the runs shows clear indications of episodic mixing as evident from the observations, suggesting that WRF may continuously mix momentum into the boundary layer. Comparing all model simulations (not shown), the erosion of the LLJ is well represented in all model simulations, but there are noticeable differences between the set-ups in the timing of the erosion and the efficiency of the momentum transport.

As introduced in section 1, the formation of the nocturnal LLJ frequently results from an inertial oscillation. Hodographs illustrating the evolution of the wind components (u and v) are shown for the night from 8–9 November 2006 for Niamey in Figure 8(d) and (e). Here, only results for the PX-41 12 km runs are shown as examples. Relatively large differences in shape and wind vector components are evident for the different driving data sets ERA (Figure 8(d)) and GFS (Figure 8(e)). Already the inital conditions at 1800 UTC show a bias between the two model runs with stronger northern wind component for the GFS run. Regarding the shape of the hodograph, the run driven by GFS fields is closer to an oscillation than the hodograph calculated from the ERA-driven run, which is more distorted. This is consistent with higher wind speeds within the LLJ layer and more downward mixing during the night, which could explain the kink at 0000 UTC (Figure 8(d)).

Also, the other WRF simulations clearly indicate the inertial oscillation and thus show the ability of the model set-ups to capture the formation of the nocturnal LLJ as outlined above. Nevertheless, although the shape of the hodographs for set-ups driven by the same boundary data is similar, the difference in strength of the individual wind speed components, resulting in

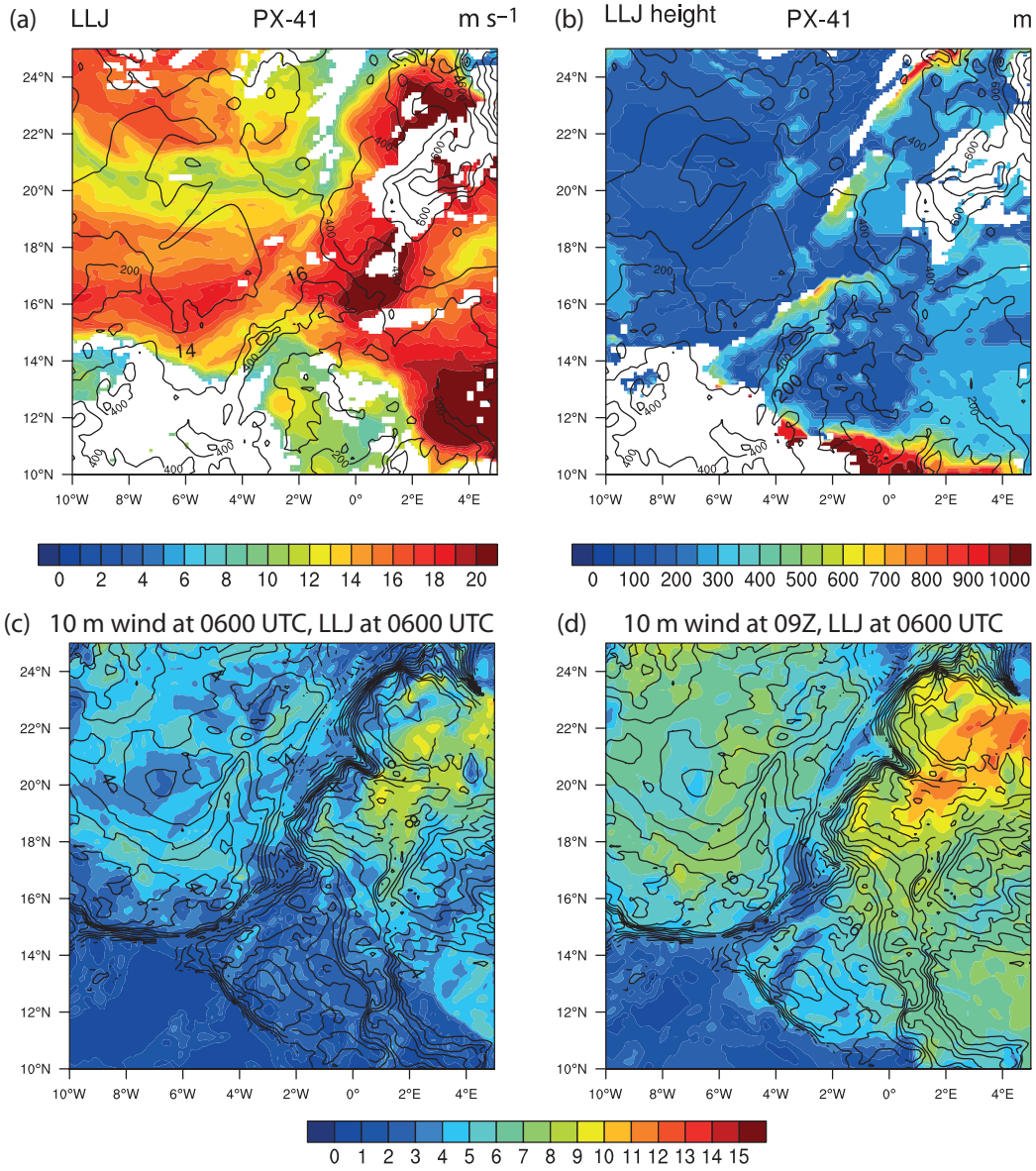

Figure 5. (a) Distribution of LLJs with core wind speeds for 9 November 2006, 0600 UTC for PX-41 run at 12 km horizontal grid driven by ERA-Interim. (b) Mean height above ground level of identified LLJs. Contour lines in (a) and (b) show orography in 100 m intervals. (c) 10 m wind speeds at 0600 UTC and (d) 10 m wind speeds at 0900 UTC. Overlaid contours represent the mean LLJ core wind speed at 0600 UTC, as shown in (a).

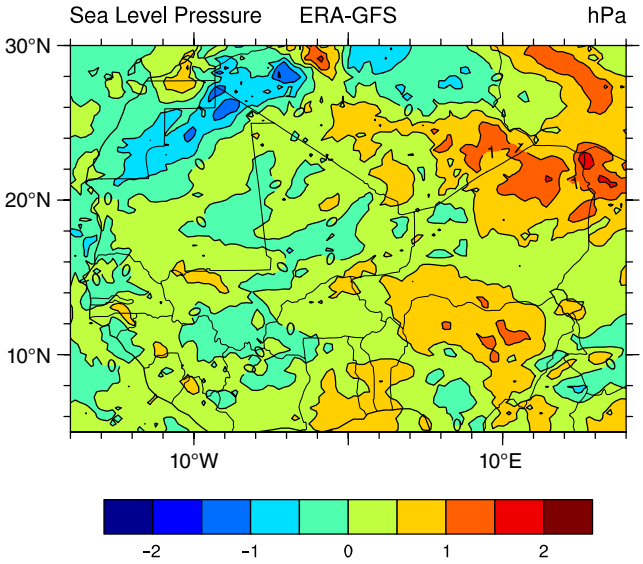

Figure 6. Difference between sea level pressure fields (hPa) for 9 November 2006 taken from PX-41 12 km simulations driven by ERA-Interim fields and GFS fields.

different shapes, is evident. The different treatment of the inertial oscillation by the different set-ups may be influenced by the different boundary-layer schemes. However, the difference in representing the inertial oscillation is larger between the ERA and the GFS set-ups than the choice of the individual boundary layers and the oscillation is more distorted in runs driven by ERA fields.

4.3. *Comparison with ground observations*

4.3.1. *Diurnal evolution*

Figure 9 shows the diurnal evolution at the three ground stations Agoufou, Bamba and Banizoumbou, comparing the observations already discussed in section 3 (cf. Figure 4) with results from the 12 km runs using the two different driving data sets. Results for the 36 and 4 km runs show similar results and thus the 12 km runs will be discussed as examples in the following. Note that the model fields are written out at one-hourly resolution, whereas the observational data are shown at 15 min intervals. Observations at Agoufou and Bamba are made at 3 m agl, whereas observations at Banizoumbou are made at 2 m agl. For comparison, model fields are extrapolated to these levels as described in section 2.1.

Generally, all model set-ups capture the general increase in near-surface wind speeds in the morning and reduction in the evening well, but there are marked differences in terms of

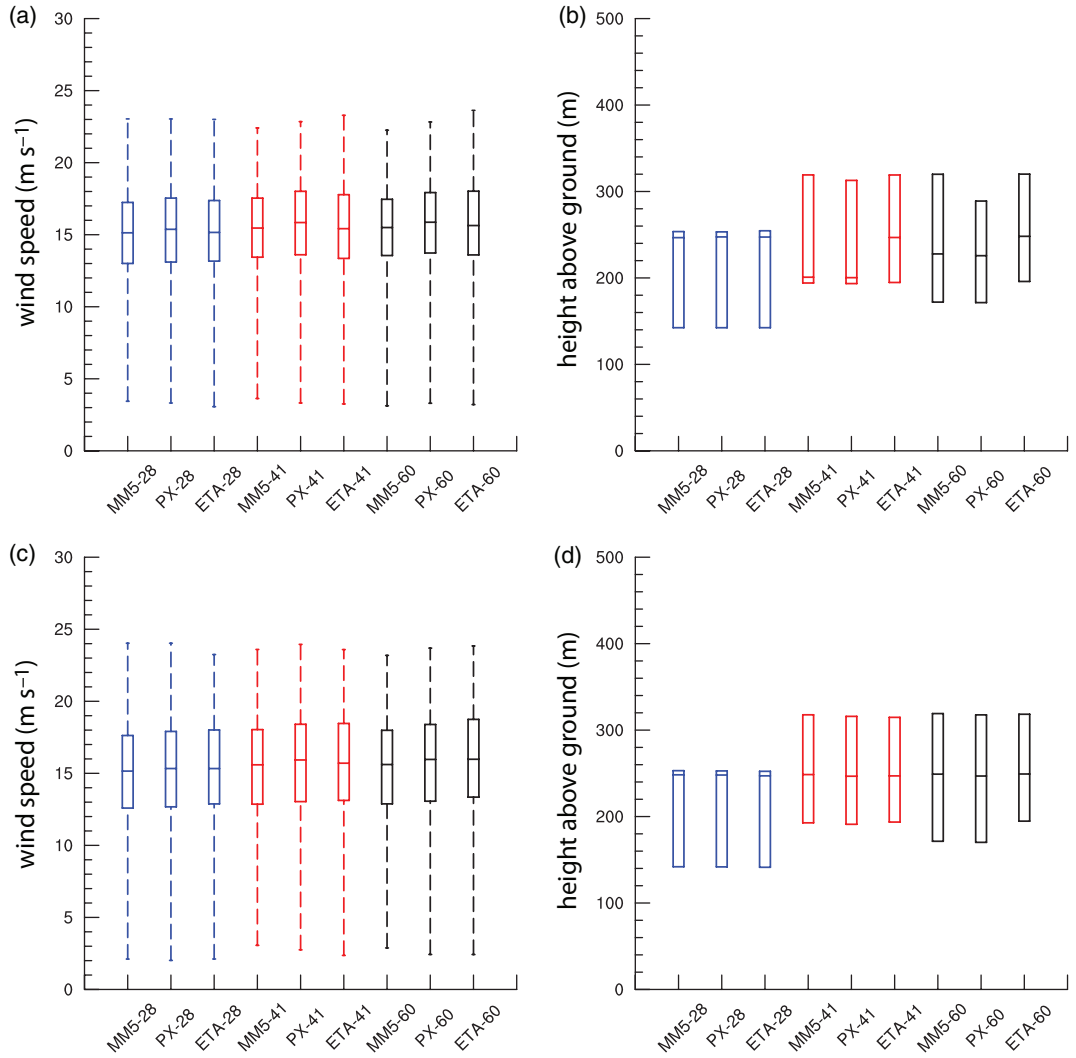

Figure 7. Spatial statistics (10°W–10°E and 10–25°N) for 9 November 2006 for (a) and (c) LLJ core wind speed and (b) and (d) LLJ core height above ground, for 0600 UTC and for all WRF set-ups initialized with (a) and (b) ERA-Inteirm and (c) and (d) GFS. The boxes are limited by 25th and 75th percentiles; the median values are represented by horizontal lines. For LLJ core wind speeds, the range of values limited by the minimum and maximum is indicated by dashed lines.

timing and magnitude of these changes, in particular for Bamba and Banizoumbou. For Agoufou (Figure 9(a) and (b)), all set-ups reproduce the decoupling and thus calm wind conditions at night reasonably well. Daytime wind speed maxima are overestimated by about 1–2 m s^{-1} using ERA-Interim fields with small differences between the set-ups and different vertical levels (Figure 9(a)), while the evening transition at 1800 UTC is generally timed well. The overestimation of wind speeds is smaller in GFS runs (Figure 9(b)).

For Bamba and ERA-Interim initial conditions (Figure 9(c)), wind speeds are generally too low except during the afternoon. The model tends to underestimate winds at night, a delayed morning transition and too low peak winds. Using GFS data as boundary conditions (Figure 9(d)), the first half of the day is matched better, including the morning wind speed maximum (particularly the runs using ACM2). In the second half of the day, degradation occurs and the simulated wind speeds decrease much faster over the course of the day than observed. As discussed above, differences from using varying driving datasets are dominating over those associated with changing set-ups and resolutions.

At Banizoumbou (Figure 9(e) and (f)), large discrepancies between model simulations and observations occur. The decoupling at night is modelled systematically as too weak, the morning transition is modelled too early and daytime winds are modelled as too strong by more than 2 m s^{-1}, while the evening transition is timed well. These results suggest that the representation of local conditions and the driving reanalysis have a significant impact on reproducing the level of agreement between model output and observations.

4.3.2. *Taylor diagrams*

Taylor diagrams (Taylor, 2001) are commonly used for comparing time series obtained from simulations with observed time series. A Taylor diagram graphically summarizes how well the datasets under study agree by showing temporal correlations and the root-mean-square difference (RMSD, proportional to the distance from the open circle marked on the *x*-axis) between the two datasets as well as the standard deviation of the model data. Simulated time series that match well with the observations lie close to the open circle on the *x*-axis (correlation close to 1, low RMSD, similar standard deviations). The curve through this open circle indicates a similar amplitude of variations (standard deviation) but a different temporal evolution. Systematic offsets are generally not represented by this method, due to subtractions of the means beforehand.

Taylor diagrams for the three observation sites Agoufou, Bamba and Banizoumbou and all 27 WRF simulations give a useful overview of the model performance (Figure 10). Generally speaking, differences between stations (rows in Figure 10) and between initiation fields (columns in Figure 10) are larger than those between different model resolutions and set-ups (spread in each panel), underlining the importance of external drivers and local conditions already discussed for Figure 9.

The overall best performance is found for Agoufou initialized with ERA-Interim data (Figure 10(a)). Correlation coefficients for all set-ups are above 0.95 and the different set-ups are only slightly above the observed standard deviation. Best matches are found for simulations using the MYJ-ETA set-up at 12 km and 27

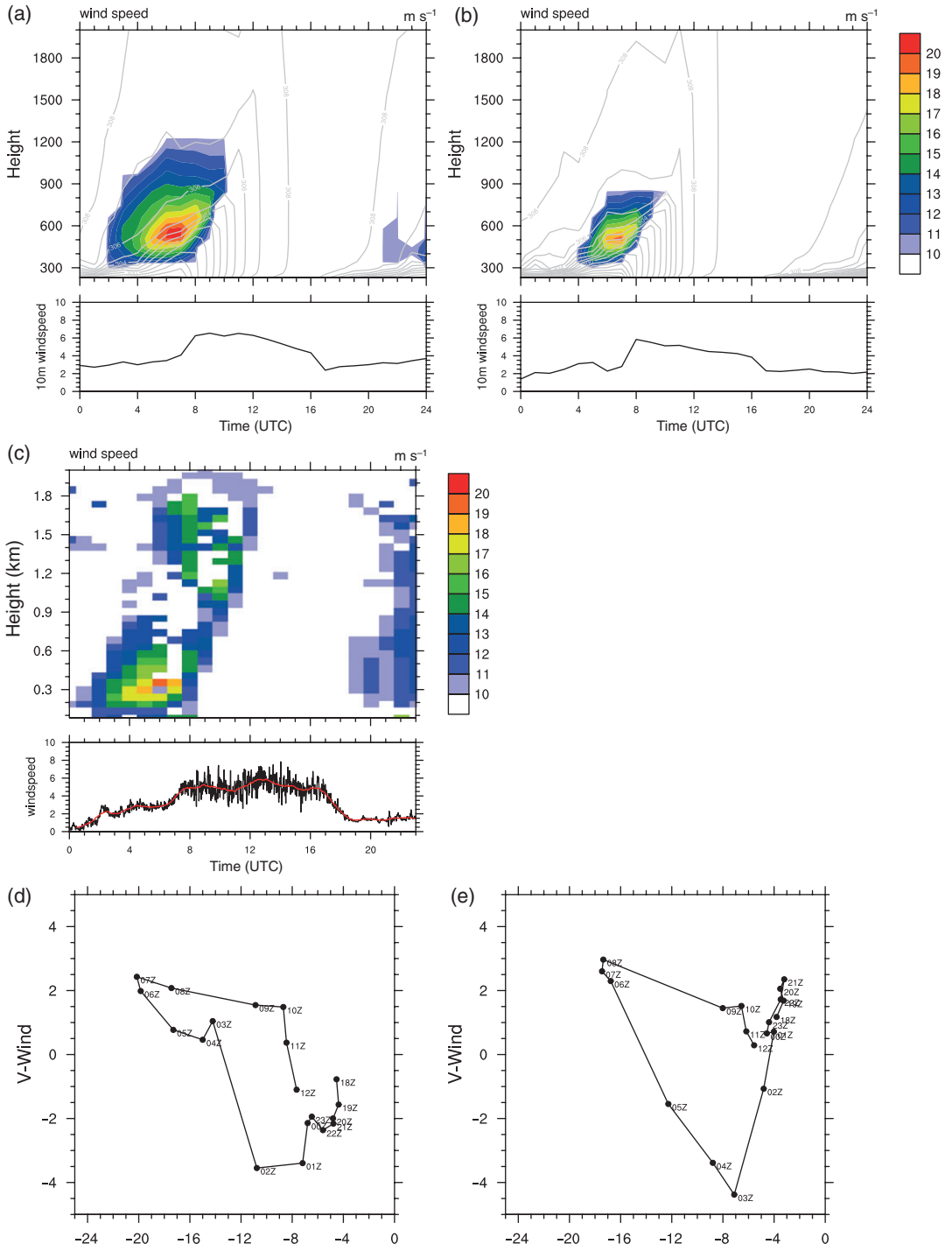

Figure 8. (a) Vertical distribution of horizontal wind speed ($m\,s^{-1}$) (colours) and potential temperature (K) (contour lines) for the PX41 12 km simulation initiated with ERA-Interim reanalysis fields for the model grid cell including Niamey, 9 November 2006. (b) Same as in (a) but for the simulation driven with GFS fields. (c) Vertical distribution of wind speeds observed by ARM facility as shown in Figure 3. (d) Hodographs of 950 hPa wind speed (LLJ core layer) for PX-41 12 km simulations initiated with ERA-Interim reanalysis fields and (e) GFS analysis fields for the model grid cell including Niamey, 9 November 2006.

levels (correlation coefficients around 0.99). These simulations also show an accurate standard deviation and low RMSD. The corresponding analysis for simulations initialized by GFS fields (Figure 10(b)) shows a general shift to lower correlations (0.95–0.99) for ACM2-PX simulations and the spread among the different set-ups is larger. The positions of the different resolutions and set-ups with respect to each other change when moving from ERA-Interim to GFS, in particular for set-ups using the ACM2 BL scheme. Notably, the MYJ-ETA set-up at 36 km and 28 levels, which is the coarsest grid resolution in this study, correlates best with the observations and has the lowest RMSD in Figure 10(b).

For Bamba (Figure 10(c) and (d)), RMSDs are generally higher and correlations lower compared with the results for Agoufou. Standard deviations tend to be too large, due to some runs showing too strong a decoupling during the night, which is partly compensated by an underestimation of the daytime maximum (Figure 9(c) and (d)). Correlations are below 0.9 for all set-ups (Figure 10(c)). However, this same configuration shows one of the best performances when GFS data are used for initialization (Figure 10(d)). The simulations initiated with GFS fields show a somewhat better correlation overall (scattered around 0.9), with the MYJ-ETA set-up matching the observed standard deviation best (correlation coefficient 0.86).

For Banizoumbou and simulations driven by ERA-Interim data (Figure 10(e)), the standard deviation is also well reproduced for MYJ set-ups, but offsets are evident for ACM2 simulations. Here, the MYJ-ETA set-up matches the observations best with regard to correlation (up to 0.87), standard deviation and RMSD. The standard deviation of the simulations initiated with GFS

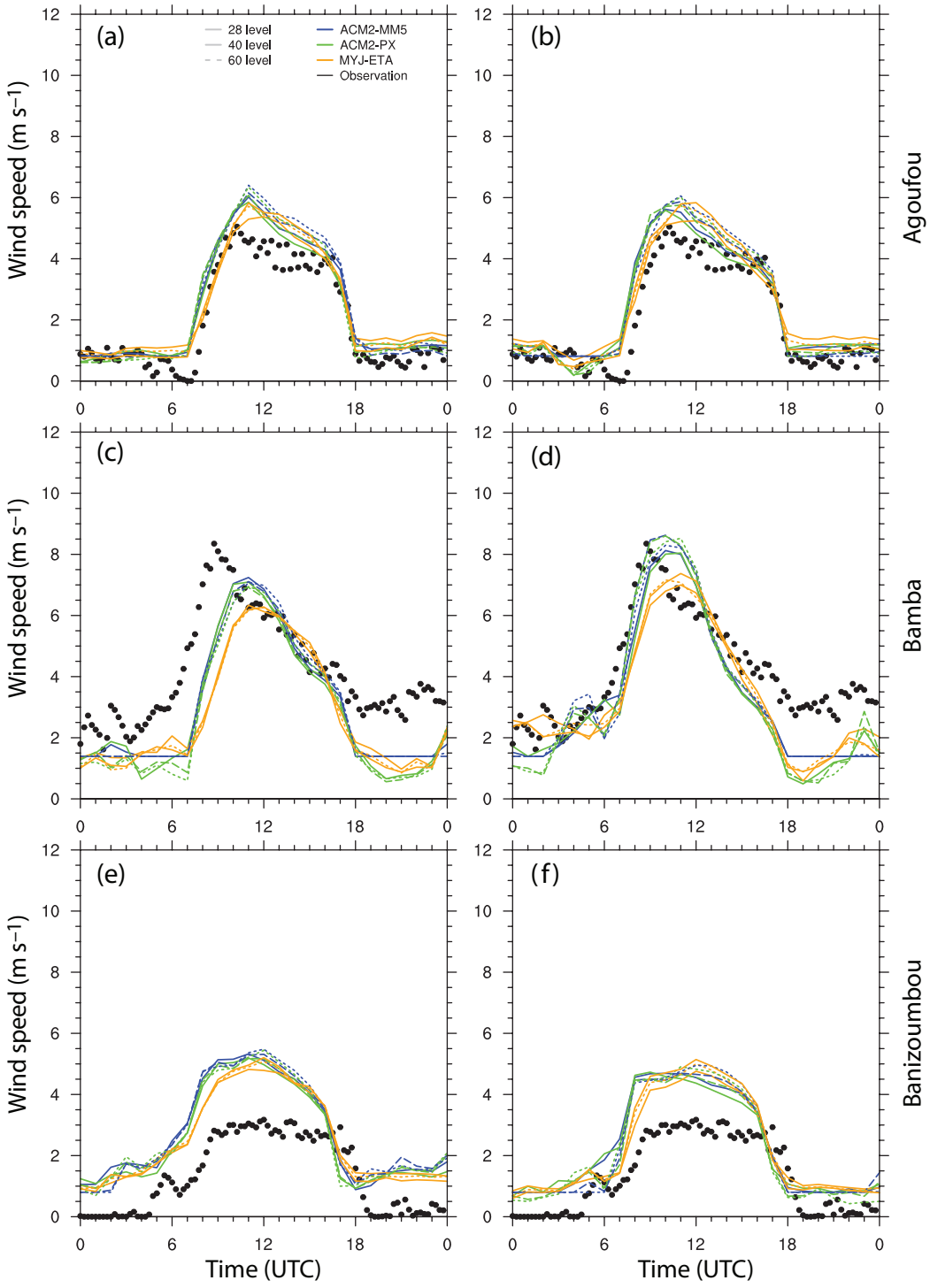

Figure 9. Time series of 3 m wind speeds (Agoufou, Bamba) and 2 m wind speeds (Banizoumbou), respectively, observed at and simulated for (a) and (b) Agoufou, (c) and (d) Bamba and (e) and (f) Banizoumbou for 9 November 2006. Simulations are driven by (a), (c) and (e) ERA-Interim fields and (b), (d) and (f) GFS analysis fields and run at the 12 km grid.

fields (Figure 10(f)) is slightly larger than the observed standard deviation and correlations are large, with values around 0.9.

Overall, there is a general tendency for the runs using different horizontal/vertical resolutions to behave similarly and appear as 'clusters' in the plots, but the choice of BL/SL scheme can make a difference in some cases, in both positive and negative ways. The same holds for differences between ERA-Interim and GFS, which are evident for all three stations.

5. Discussion and conclusions

In this study, a set of 27 simulations using the WRF model is investigated to assess the representation of LLJs over West Africa and its sensitivity to model configuration for a dry-season case study on 9 November 2006, when additional observations as part of the AMMA field campaign are available for model evaluation. LLJs in this region are important for dust emission and transport. This case study was selected as it represents a typical dry-season situation with a marked pressure gradient across northern Africa and strong northeasterly to easterly Harmattan flow. The simulations were grouped into three different sets of experiments, with varying (i) initial and boundary data (ERA-Interim versus GFS), (ii) BL/SL schemes (three different combinations, representative of non-local and local BL schemes) and (iii) horizontal (36, 12 and 4 km) and vertical (28, 41 and 60 levels) grid spacings. The results were analyzed and discussed with respect to the typical life cycle of LLJs related to a nocturnal decoupling and inertial oscillation.

Generally speaking, all model configurations are capable of reproducing the overall characteristics of LLJ formation and

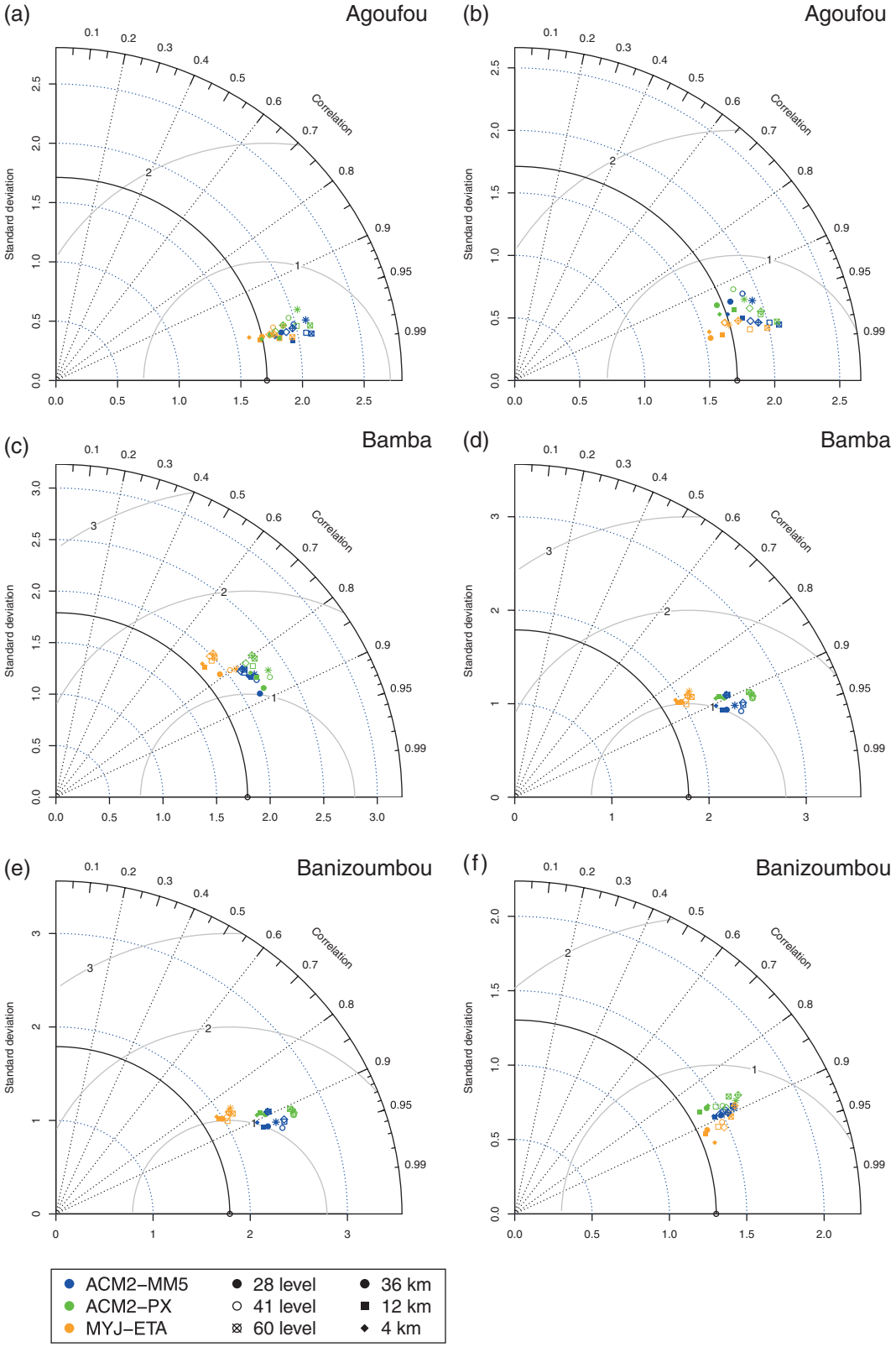

Figure 10. Taylor diagrams for (a) and (b) Agoufou, (c) and (d) Bamba and (e) and (f) Banizoumbou, comparing the near-surface wind observations with WRF simulations from the different experiments. Panels (a), (c) and (e) show model set-ups initialized with ERA-Interim reanalysis fields, panels (b), (d) and (f) model set-ups initialized with GFS analysis fields. The legend is as follows. The colour represents the BL/SL set-up (ACM2-MM5, ACM2-PX, MYJ-ETA), the shape of the symbol represents the horizontal grid spacing (36, 12, 4 km) and the fill (solid, open, crossed) represents the number of levels.

breakdown. The high-resolution simulations show a complicated spatial pattern of LLJ core wind speed over the Sahel and southern Sahara characterized by the strongest LLJs across parts of the Sahel and in the vicinity of the Hoggar and Adrar des Iforhas Mountains, but weak LLJs to the south of the sharp Harmattan front and in a north–south oriented confluence zone related to Saharan topography. No strong LLJs were identified over higher ground, most likely due to disturbances to the development of a stable nocturnal boundary layer by topographic effects. Typical LLJ core speeds are 15 m s^{-1} at heights between 200 and 250 m above ground. The breakdown of these jets in the morning causes an increase in 10 m wind speed over the entire domain between 0600 and 0900 UTC. Such behaviour is also evident from ground stations, radiosondes and wind radar measurements.

In contrast to some previous studies on LLJs in other regions, the greatest sensitivities are found with respect to the initialization and boundary data, which deviate locally by as much as 6 gpm in 925 hPa geopotential height. The choice of driving data affects

local LLJ speed, height, depth and the timing of decoupling and jet breakdown, finally also affecting the temporal evolution and strength of surface wind speeds such as the morning and evening transition and daily maximum. Averaged over the entire model domain, however, differences in LLJ statistics are not very large, probably due to cancellation effects. Nevertheless, these results demonstrate the considerable uncertainty related to the lack of observational constraint for analyses caused by the sparse observational network over large parts of northern Africa, making this aspect more prominent here than in other regions. Compared with this, sensitivities with regard to horizontal and vertical resolution and parametrizations are small and do not show systematic patterns.

Detailed comparisons with the time evolution at individual surface stations using Taylor diagrams and other diagnostics show considerable differences between the stations. These occur in both directions and are typically larger than the differences between individual simulations. This suggests that local conditions around the stations, for example related to roughness, albedo or soil moisture, are not well represented in the model, or that those stations are not representative of the surrounding area on the scale of the model grid box.

Several extensions to this work are conceivable. Despite the careful selection of the case study to represent typical conditions during the dry season, a more systematic analysis spanning a longer time period is desirable. Results from this study illustrate that a major limitation to accurate mesoscale modelling and therefore forecasting over the Sahel is the uncertainty associated with the datasets used for initializing and driving the simulations. To overcome this problem, improvements are needed to both modelling and observational components of the analysis system. It can be assumed that an increased use of satellite information and an expansion of conventional observations in this region would help to improve the situation, along with improvements of global models in representing key atmospheric processes over northern Africa and the surrounding waters. Finally, the role of local conditions such as roughness and albedo should be tested systematically through comparison between model variables and observations from ground and satellite, as well as through model sensitivity studies. These together will help us better to evaluate and improve model performance in the future, through a better separation of the different contributing factors such as surface characteristics, boundary-layer dynamics and background atmospheric flow.

Acknowledgements

This study was funded under the European Research Council grant 257543 'Desert Storms'. The US Department of Energy as part of the Atmospheric Radiation Measurement (ARM) Climate Research Facility has funded the deployment of the ARM Mobile Facility (AMF) in Niamey, Niger, as part of the AMMA (African Monsoon Multidisciplinary Analysis) and GERB (Global Earth Radiation Budget) projects. The deployment of the ground observation sites in Agoufou, Bamba and Banizoumbou and the radiosonde launched at Niamey were funded through the AMMA initiative. ERA-Interim reanalysis fields were made available through the ECMWF, GFS analysis fields were available through NOAA. The authors thank Steven Pickering (University of Leeds, UK) for his help with running the WRF model on the ARC1 supercomputer. The authors thank the Editor Doug Parker, the Associate Editor Gert-Jan Steeneveld and five anonymous reviewers for fruitful and helpful discussions that helped to improve an earlier version of this manuscript significantly.

References

Baas P, Bosveld FC, Lenderink G, van Meijgaard E, Holtslag AAM. 2010. How to design single-column model experiments for comparison with observed nocturnal low-level jets. *Q. J. R. Meteorol. Soc.* **136**: 671–684, doi: 10.1002/qj.592.

Banta RM, Senff CJ, White AB, Trainer M, McNider RT, Valente RJ, Mayor SD, Alvarez RJ, Hardesty RM, Parish DD, Fehsenfeld FC. 1998. Daytime buildup and nighttime transport of urban ozone in the boundary layer during a stagnation episode. *J. Geophys. Res.* **103**: 22519–22544, doi: 10.1029/98JD01020.

Banta RM, Pichugina YL, Brewer WA. 2006. Turbulent velocity-variance profiles in the stable boundary layer generated by a nocturnal low-level jet. *J. Atmos. Sci.* **63**: 2700–2719.

Blackadar AK. 1957. Boundary layer wind maxima and their significance for the growth of nocturnal inversions. *Bull. Am. Meteorol. Soc.* **38**: 283–290.

Borge R, Alexandrov V, del Vas JJ, Lumbreras J, Rodriguez E. 2008. A comprehensive sensitivity analysis of the WRF model for air quality applications over the Iberian Peninsula. *Atmos. Environ.* **42**: 8560–8574, doi: 10.1016/j.atmosenv.2008.08.032.

Bouet C, Cautenet G, Washington R, Todd MC, Laurent B, Marticorena B, Bergametti G. 2007. Mesoscale modeling of aeolian dust emission during the BoDEx 2005 experiment. *Geophys. Res. Lett.* **34**: L07812, doi: 10.1029/2006GL029184.

Burton R, Devine GM, Parker DJ, Chazette P, Dixon N, Flamant C, Haywood JM. 2013. The Harmattan over West Africa: Nocturnal structure and frontogenesis. *Q. J. R. Meteorol. Soc.* **139**: 1364–1373, doi: 10.1002/qj.2036.

Cappelaere B, Descroix L, Lebel T, Boulain N, Ramier D, Laurent J-P, Favreau G, Boubkraoui S, Boucher M, Moussa IB, Chaffard V, Hiernaux P, Issoufou HBA, Le Breton E, Mamadou I, Nazoumou Y, Oi M, Ottle C, Quantin G. 2009. The AMMA–CATCH experiment in the cultivated Sahelian aera of south-west Niger –Investigating water cycle response to a fluctuating climate and changing environment. *J. Hydrol.* **375**: 34–51, doi: 10.1016/j.jhydrol.2009.06.021.

Chen F, Dudhia J. 2001. Coupling an advanced land surface-hydrology model with the Penn State–NCAR MM5 modeling system. Part I: Model description and implementation. *Mon. Weather Rev.* **129**: 569–585.

Chiao S, Dumais R. 2013. A down-valley low-level jet event during T-REX 2006. *Meteorol. Atmos. Phys.* **122**: 75–90, doi: 10.1007/s00703-013-0279-z.

Dee DP, Uppala SM, Simmons A, Berrisford P, Poli P, Kobayashi S, Andrae U, Balmaseda MA, Balsamo G, Bauer P, Bechtold P, Beljaars ACM, van de Berg L, Didlot J, Bormann N, Delsol C, Dragani R, Fuentes M, Geer AJ, Haimberger L, Healy SB, Hersbach H, Holm EV, Isaksen L, Kallberg P, Kohler M, Matricardi M, McNally AP, Monge-Sanz BM, Morcrette J-J, Park BK, Peubey C, de Rosnay P, Tavolato C, Thepaut JN, Vitart F. 2011. The ERA-Interim reanalysis: Configuration and performance of the data assimilation system. *Q. J. R. Meteorol. Soc.* **137**: 553–597, doi: 10.1002/qj.828.

Dudhia J. 1989. Numerical study of convection observed during the winter monsoon experiment using a two-dimensional model. *J. Atmos. Sci.* **46**: 3077–3107.

Fiedler S, Schepanski K, Heinold B, Knippertz P, Tegen I. 2013. Climatology of nocturnal low-level jets over North Africa and implications for modeling mineral dust emission. *J. Geophys. Res.* **118**: 6100–6121, doi: 10.1002/jgrd.50394.

Giannakopoulou EM, Toumi R. 2012. The Persian Gulf summertime low-level jet over sloping terrain. *Q. J. R. Meteorol. Soc.* **138**: 145–157, doi: 10.1002/qj.901.

Gibbs JA, Fedorovich E, van Eijk AMJ. 2011. Evaluating weather research and forecasting (WRF) model predictions of turbulent flow parameters in a dry convective boundary layer. *J. Appl. Meteorol. Climatol.* **50**: 2429–2444, doi: 10.1175/2011JAMC2661.1.

Gilliam RC, Pleim JE. 2009. Performance assessment of new land surface and planetary boundary layer physics in the WRF–ARW. *J. Appl. Meteorol. Climatol.* **49**: 760–774, doi: 10.1175/2009JAMC2126.1.

Hanna SR, Yang R. 2001. Evaluations of mesoscale models' simulations of near-surface winds, temperature gradients, and mixing depths. *J. Appl. Meteorol.* **40**: 1095–1104.

Heinold B, Knippertz P, Marsham JH, Fiedler S, Dixon NS, Schepanski K, Laurent B, Tegen I. 2013. The role of deep convection and nocturnal low-level jets for dust emission in summertime West Africa: Estimates from convection-permitting simulations. *J. Geophys. Res.* **118**: 4385–4400, doi: 10.1002/jgrd.50402.

Horvath K, Koracin D, Vellore R, Jiang J, Belu R. 2012. Sub-kilometer dynamical downscaling of near-surface winds in complex terrain using WRF and MM5 mesoscale models. *J. Geophys. Res.* **117**: D11111, doi: 10.1029/2012JD017432.

Hu X-M, Nielsen-Gammon JW, Zhang F. 2010. Evaluation of three planetary boundary layer schemes in the WRF model. *J. Appl. Meteorol. Climatol.* **49**: 1831–1844, doi: 10.1175/2010JAMC2432.1.

Hu X-M, Doughty DC, Sanchez KJ, Joseph E, Fuentes JD. 2012. Ozone variability in the atmospheric boundary layer in Maryland and its implications for vertical transport model. *Atmos. Environ.* **46**: 354–364, doi: 10.1016/j.atmosenv.2011.09.054.

Hu X-M, Klein PM, Xue M. 2013. Evaluation of the updated YSU planetary boundary layer scheme within WRF for wind resource and air quality assessments. *J. Geophys. Res.* **118**: 490–505, doi: 10.1002/jgrd.50823.

Janjic ZI. 2001. 'Nonsingular implementation of the Mellor–Yamada level 2.5 scheme in the NCEP mesomodel', NCEP Office Note No. 437. National Centers for Environmental Prediction: Camp Springs, MD.

Kalu AE 1979. The African dust plume: Its characteristics and propagation across West Africa in winter. *SCOPE* **14**: 95–118.

Kleczek MA, Steeneveld G-J, Holtslag AAM. 2014. Evaluation of the weather research and forecasting mesoscale model for GABLS3: Impact of boundary-layer schemes, boundary conditions and spin-up. *Boundary Layer Meteorol.* **152**: 213–243, doi: 10.1007/s10546-014-9925-3.

Knippertz P. 2008. Dust emission in the West African heat trough –the role of the diurnal cycle and of extratropical distrubances. *Meteorol. Z.* **17**: 553–563, doi: 10.1127/0941-1948/2008/0315.

Knippertz P, Todd MC. 2012. Mineral dust aerosols over the Sahara: Meteorological controls on emission and transport and implications for modeling. *Rev. Geophys.* **50**: RG1007, doi: 10.1029/2011RG000362.

Kothe S, Lüthi D, Ahrens B. 2013. Analysis of the West African Monsoon system in the regional climate model COSMO-CLM. *Int. J. Climatol.* **34**: 481–493, doi: 10.1002/joc.3702.

Li X, Pu Z. 2008. Sensitivity of numerical simulations of early rapid intensification of Hurricane Emily (2005) to cloud microphysical and planetary boundary layer parametrizations. *Mon. Weather Rev.* **136**: 4819–4838, doi: 10.1175/2008MWR2366.1.

Liechti F, Schaller E. 1999. The use of low-level jets by migrating birds. *Naturwissenschaften* **86**: 549–551.

Maddox RA. 1983. Large-scale meteorological conditions associated with midlatitutde mesoscale convective complexes. *Mon. Weather Rev.* **111**: 1475–1493.

Menut L. 2008. Sensitivity of hourly Saharan dust emissions to NCEP and ECMWF modeled wind speed. *J. Geophys. Res.* **113**: D16201, doi: 10.1029/2007JD009522.

Miller MA, Slingo A. 2007. The ARM Mobile Facility and its first international deployment: Measuring radiative flux divergence in West Africa. *Bull. Am. Meteorol. Soc.* **88**: 1229–1244, doi: 10.1175/BAMS-88-8-1229.

Mlawer EJ, Taubman SJ, Brown PD, Iacono MJ, Clough SA. 1997. Radiative transfer for inhomogeneous atmospheres: RRTM, a validated correlated-k model for long-wave. *J. Geophys. Res.* **102**: 16663–16682, doi: 10.1029/97JD00237.

Mougin E, Hiernaux P, Kergoat L, Grippa M, de Rosnay P, Timouk F, Le Dantec V, Demarez V, Lavenu F, Arjounin M, Lebel T, Soumaguel N, Ceschia E, Mougenot B, Baup F, Frappart F, Frison PL, Gardelle J, Gruhier C, Jarlan L, Mangiarotti S, Sanou B, Tracol Y, Guichard F, Trichon V, Diarra L, Soumaré A, Koité M, Dembélé F, Lloyd C, Hanan NP, Damesin C, Delon C, Serca D, Galy-Lacaux C, Seghieri J, Becerra S, Dia H, Gangneron F, Mazzega P. 2009. The AMMA–CATCH Gourma observatory site in Mali: Relating climatic variations to changes in vegetation, surface hydrology, fluxes and natural resources. *J. Hydrol.* **375**: 14–33, doi: 10.1016/j.hydrol.2009.06.045.

Ngan F, Hyuncheol K, Lee P, Al-Wali K, Dornblaser B. 2013. A study of nocturnal surface wind speed overprediction by the WRF–ARW Model in Southeastern Texas. *J. Appl. Meteorol. Climatol.* **52**: 2638–2653, doi: 10.1175/JAMC-D-13-060.1.

Nielsen-Gammon JW, Hu X-M, Zhang F, Pleim JE. 2010. Evaluation of planetary boundary layer scheme sensitivities for the purpose of parameter estimation. *Mon. Weather Rev.* **138**: 3400–3417, doi: 10.1175/2010MWR3292.1.

Paulson CA. 1970. The mathematical representation of wind speed and temperature profiles in the unstable atmospheric surface layer. *J. Appl. Meteorol.* **9**: 857–861.

Pleim J. 2006. A simple, efficient solution of flux-profile relationships in the atmospheric surface layer. *J. Appl. Meteorol. Climatol.* **45**: 341–347.

Pleim J. 2007. A combined local and nonlocal closure model for the atmospheric boundary layer. Part I: Model description and testing. *J. Appl. Meteorol. Climatol.* **46**: 1383–1395.

Poulos GS, Blumen W, Frittas DC, Lundquist JK, Sun J, Burns SP, Nappo C, Banta R, Newsom R, Cuyart J, Terradellas E, Balsley B, Jensen M. 2002. CASES-99: A Comprehensive Investigation of the Stable Nocturnal Boundary Layer. *Bull. Am. Meteorol. Soc.* **88**: 555–581.

Redelsperger J-L, Thorncroft CD, Diedhiou A, Lebel T, Parker DJ, Polcher J. 2006. African monsoon multidisciplinary analysis: An interantional research project and field campaign. *Bull. Am. Meteorol. Soc.* **87**: 1739–1746, doi: 10.1175/BAMS-87-12-1739.

Schepanski K, Tegen I, Todd MC, Heinold B, Bönisch G, Laurent B, Macke A. 2009a. Meteorological processes forcing Saharan dust emission inferred from MSG–SEVIRI observations of sub-daily dust source activation and numerical models. *J. Geophys. Res.* **114**: D10201, doi: 10.1029/2008JD010325.

Schepanski K, Tegen I, Macke A. 2009b. Saharan dust transport and deposition towards the tropical northern Atlantic. *Atmos. Chem. Phys.* **9**: 1173–1189.

Schepanski K, Flamant C, Chaboureau J-P, Kocha C, Banks JR, Brindley HE, Lavaysse C, Marnas F, Pelon J, Tulet P. 2013. Characterization of dust emission from alluvial sources using aircraft observations and high-resolution modeling. *J. Geophys. Res.* **118**: 7237–7259, doi: 10.1002/jgrd.50538.

Shin HH, Hong S-Y. 2011. Intercomparison of planetary boundary-layer parametrizations in the WRF model for a single day from CASES-99. *Boundary Layer Meteorol.* **139**: 261–281, doi: 10.1007/s10546-010-9583-z.

Skamarock WC, Klemp JB, Dudhia J, Gill DO, Barker DM, Duda MG, Huang X-Y, Wang W, Powers JG. 2008. 'A description of the advanced research WRF version 3', Technical Note NCAR/TN-475+STR. National Center for Atmospheric Research (NCAR): Boulder, CO.

Slingo A, Bharmal NA, Robinson GJ, Settle JJ, Allan RP, White HE, Lamb PJ, Issa Lélé M, Turner DD, McFarlane S, Kassianov E, Barnard J, Flynn C, Miller M. 2008. Overview of observations from the RADAGAST experiment in Niamey, Niger: Meteorology and thermodynamic variables. *J. Geophys. Res.* **113**: D00E01, doi: 10.1029/2008JD009909.

Stensrud DJ. 1996. Importance of low-level jets to climate: A review. *J. Clim.* **9**: 1698–1711.

Storm B, Basu S. 2010. The WRF model forecast-derived low-level wind shear climatology over the United States Great Plains. *Energies* **3**: 258–276, doi: 10.3390/en3020258.

Storm B, Dudhia J, Basu S, Swift A, Giammanco I. 2009. Evaluation of the weather research and forecasting model on forecasting low-level jets: Implications for wind energy. *Wind Energy* **12**: 81–90, doi: 10.1002/we.288.

Stull RB. 1989. *An Introduction to Boundary Layer Meteorology*. Kluwer Academic Publishers: Dordrecht, the Netherlands, Boston, MA and London.

Sun J, Lenschow DH, Mahrt L, Nappo C. 2013. The relationships among wind, horizontal pressure gradient, and turbulent momentum transport during CASE-99. *J. Atmos. Sci.* **70**: 3397–3414, doi: 10.1175/JAS-D-12-0233.1.

Taylor KE. 2001. Summarizing multiple aspects of model performance in a single diagram. *J. Geophys. Res.* **106**: 7183–7192, doi: 10.1029/2000JD900719.

Tegen I, Schepanski K, Heinold B. 2013. Comparing two years of Saharan dust source activation obtained by regional modelling and satellite observations. *Atmos. Chem. Phys.* **13**: 2381–2390, doi: 10.5194/acp-13-2381-2013.

Thorpe AJ, Guymer TH. 1977. The nocturnal low-level jet. *Q. J. R. Meteorol. Soc.* **103**: 633–653.

Todd MC, Washington R, Martins JV, Dubovik O, Lizcano G, M'Bainayel S, Engelstaedter S. 2007. Mineral dust emission from the Bodele Depression, northern Chad, during BoDEx 2005. *J. Geophys. Res.* **112**: D06207, doi: 10.1029/2006JD007170.

Van de Wiel BJH, Moene AF, Steeneveld GJ, Baas P, Bosveld FC, Holtslag AAM. 2010. A conceptual view on intertial oscillation and nocturnal low-level jets. *J. Atmos. Sci.* **67**: 2679–2689, doi: 10.1175/2010JAS3289.1.

Washington R, Todd MC. 2005. Atmospheric controls on mineral dust emission from the Bodele Depression, Chad: The role of the low level jet. *Geophys. Res. Lett.* **32**: L17701, doi: 10.1029/2005GL023597.

Washington R, Bouet C, Cautenet G, Mackenzie E, Ashpole I, Engelstaedter S, Lizcano G, Henderson GM, Schepanski K, Tegen I. 2009. Dust as a tipping element: The Bodele Depression, Chad. *Proc. Natl. Acad. Sci. U.S.A.* **106**: 20 564–20 571, doi: 10.1073/pnas.0711850106.

Westphal DL, Toon OB, Carlson TN. 1987. A two-dimensional numerical investigation of the dynamics and microphysics of Saharan dust stroms. *J. Geophys. Res.* **92**: 3027–3049, doi: 10.1029/JD092iD03p03027.

Xie B, Hunt JCR, Carruthers DJ, Fung JCH, Barlow JF. 2013. Structure of the planetary boundary layer over Southeast England: Modeling and measurements. *J. Geophys. Res.* **118**: 7799–7818, doi: 10.1002/jgrd.50621.

Yang Q, Berg LK, Pekour M, Fast JD, Newsom RK. 2013. Evaluation of WRF-predicted near-hub-height winds and ramp events over a Pacific Northwest site with complex terrain. *J. Appl. Meteorol. Climatol.* **52**: 1753–1763, doi: 10.1175/JAMC-D-12-0267.1.

Yver CE, Graven HD, Lucas DD, Cameron-Smith PJ, Keeling RF, Weiss RF. 2013. Evaluating transport in the WRF model along the California coast. *Atmos. Chem. Phys.* **13**: 1837–1852, doi: 10.5194/acp-13-1837-2013.

Zhang D-L, Zheng W-Z. 2004. Diurnal cycles of surface winds and temperatures as simulated by five boundary layer parametrizations. *J. Appl. Meteorol.* **43**: 157–169, doi: 10.1175/1520-0450(2004)043.

Zhong S, Fast JD. 2003. An evaluation of MM5, RAMS, and Meso Eta at sub-kilometer resolution using the VTMX field campaign data in the Salt Lake Valley. *Mon. Weather Rev.* **131**: 1301–1322, doi: 10.1175/1520-0493.